Supplementary Information for

Chiral modes and directional lasing at exceptional points

Bo Peng, Şahin Kaya Özdemir*, Matthias Liertzer, Weijian Chen, Johannes Kramer, Huzeyfe Yilmaz, Jan Wiersig, Stefan Rotter, and Lan Yang*

*Corresponding author. E-mail: ozdemir@wustl.edu (S.K.O), yang@ese.wustl.edu (L.Y)

Supplementary Text

S1. Two-Mode-Approximation (TMA) model and the eigenmode evolution.

In this section we briefly review the two-mode approximation (TMA) model and the eigenmode evolution in whispering-gallery-mode (WGM) microcavities with nanoscatterer-induced broken spatial symmetry, as described briefly in the main text. This will help to understand the basic relationship between asymmetric backscattering of counter-propagating waves and the resulting co-propagation, non-orthogonality, and chirality of optical modes. We furthermore derive how the chirality of a lasing mode can be measured by weakly coupling two waveguides to the system. As a complementary schematic of the setup shown in **Fig.1** in the main text, **Fig. S1** presents the details of the involved parameters and the input/output signal directions for clarification.

The TMA model used in our analysis was first phenomenologically introduced for deformed microdisk cavities[5,8] and was later rigorously derived for the microdisk with two scatterers[1]. The main approach is to model the dynamics in the slowly-varying envelope approximation in the time domain with a Schrödinger-like equation

$$i\frac{d}{dt}\Psi = \mathrm{H}\Psi \tag{S.1}$$

Here, Ψ is the complex-valued two-dimensional vector consisting of the field amplitudes of the CCW propagating wave Ψ_{CCW} and the CW propagating wave Ψ_{CW}. The former corresponds to the $e^{im\varphi}$ angular dependence in real space, and the latter to $e^{-im\varphi}$; the positive integer m is the angular mode number. Since the microcavity is an open system, the corresponding effective Hamiltonian,

$$\mathrm{H} = \begin{pmatrix} \Omega_c & A \\ B & \Omega_c \end{pmatrix} \tag{S.2}$$

is a 2x2 matrix, which is in general non-Hermitian.

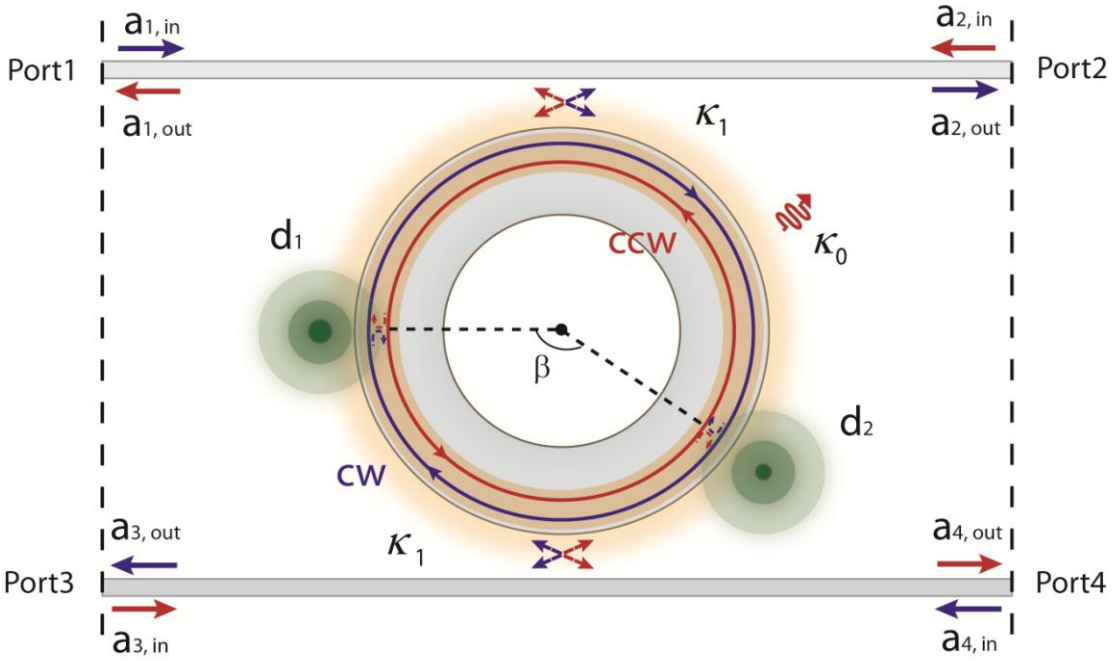

Fig. S1. *Schematic of the setup with the definitions of the parameters and signal propagation directions.* $a_{j,\mathrm{in}}$ *(*$a_{j,\mathrm{out}}$*) denotes the input (output) signal amplitude from the j-th port.* κ_0, κ_1 *are the cavity decay rate and the cavity-waveguide coupling coefficient, respectively.* d_1 *(*d_2*) denotes the effective scattering size factor of the first (second) nanoscatterer (corresponding to the spatial overlap between the scatterer and the optical mode), which is varied by changing the distance between the scatterer and the microresonator. The angle* β *denotes the relative phase angle between the scatterers.*

The real parts of the diagonal elements Ω_c are the frequencies and the imaginary parts are the decay rates of the resonant traveling waves. The complex-valued off-diagonal elements A and B are the backscattering coefficients, which describe the scattering from the CW (CCW) to the CCW (CW) travelling wave. In general, in the open system the backscattering is asymmetric, $|A| \neq |B|$, which is allowed because of the non-Hermiticity of the Hamiltonian. The complex eigenvalues of H are,

$$\Omega_{\pm} = \Omega_c \pm \sqrt{AB} \tag{S.3}$$

to which the following complex (not normalized) right eigenvectors are associated,

$$\Psi_{\pm} = \begin{pmatrix} \sqrt{A} \\ \pm\sqrt{B} \end{pmatrix}. \tag{S.4}$$

As shown in the text, the asymmetric scattering is closely related with the evolution of the eigenmodes, especially in the vicinity of the exceptional points (EP), where either of the backscattering coefficients A or B is zero and both the eigenvalues (S.3) and the eigenvectors (S.4) coalesce[2,3,9,10]. To verify this interesting feature, we specifically checked the eigenmode evolution in our system both theoretically and experimentally. For the particular case of the WGM microtoroid perturbed by two scatterers the matrix elements of H are determined as follows,

$$\begin{aligned} \Omega_c &= \Omega_0 + V_1 + U_1 + V_2 + U_2 \\ &= \omega_c - \frac{\kappa_0 + 2\kappa_1}{2} i + V_1 + U_1 + V_2 + U_2 \end{aligned} \tag{S.5}$$

$$A = (V_1 - U_1) + (V_2 - U_2) e^{-2im\beta} \tag{S.6}$$

$$B = (V_1 - U_1) + (V_2 - U_2) e^{2im\beta} \tag{S.7}$$

where ω_c denotes the intrinsic cavity resonant frequency, and κ_0 and κ_1 are the cavity decay rate and the cavity-waveguide coupling coefficient. The quantities $2V_j$ and $2U_j$ are given by the complex frequency shifts for positive- and negative-parity modes introduced by j-th particle ($j = 1, 2$) alone. These quantities can be calculated for the single-particle-microdisk system either fully numerically [using, e.g., the finite-difference

time-domain method[11] (FDTD), the boundary element method[12] (BEM)], or analytically using the Green's function approach[13] for point scatterers with $U_j = 0$. Here we used the finite element method[14] (FEM). Note that *A* or *B* can be set to zero by choosing proper values for β and for the scatterer strength V_2. In our simplified model U_j is set to zero since $|U_j| << |V_j|$.

Figure S2 presents the evolution of the eigenfrequencies of our system (obtained with FEM simulations) as the phase difference angle β and the effective size factor *d* are tuned. The EPs can be clearly observed where the eigenfrequencies coalesce, as pointed out in both **Fig.S2A** and **S2B**.

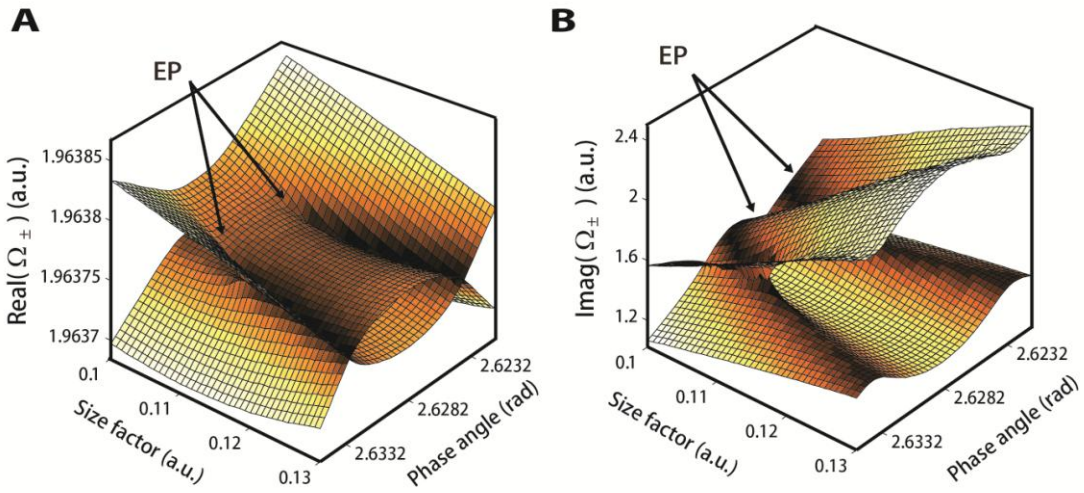

Fig. S2. *The eigenmode evolution of the non-Hermitian system as a function of the effective size factor d and the relative phase angle β between the scatterers. (A) Real part of the eigenmodes $\Omega_{\pm}$. (B) Imaginary part of the eigenmodes $\Omega_{\pm}$.Two exceptional points are clearly seen. EP: Exceptional Point.*

S2. Experimental observation of an EP by tuning the size and position of two scatterers.

In our experiments with a silica microtoroid WGM resonator, we chose a mode for which there was no observable frequency splitting in the transmission spectra before the introduction of the scatterers. We probed the scatterer-induced chiral dynamics of the

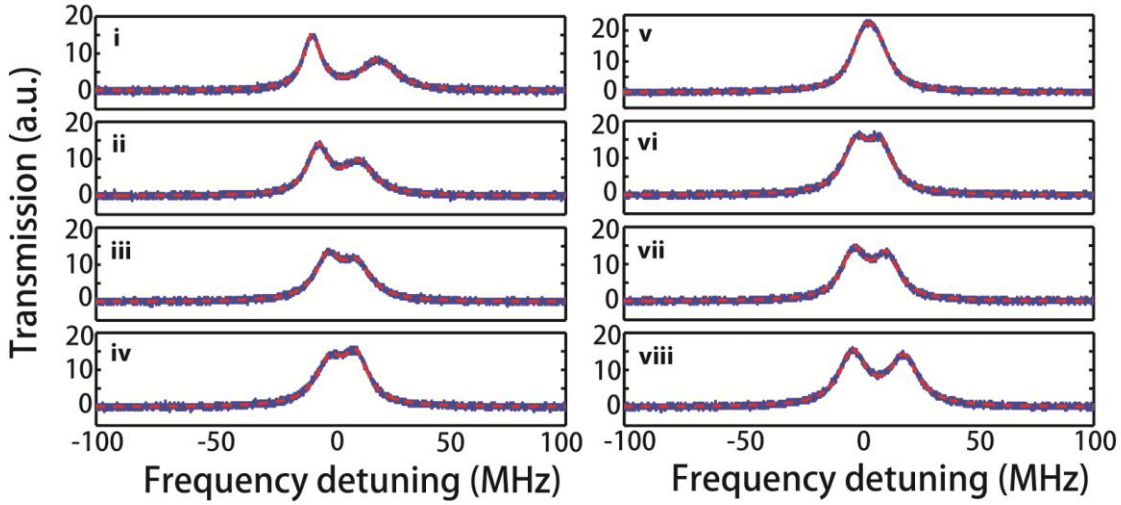

Fig. S3. *Experimentally obtained mode spectra as the relative phase angle β between the scatterers was varied. β increased continuously from (i) to (viii). Mode coalescence is clearly seen in (v). Modes bifurcated again when β was increased further (vi-viii) .*

WGMs, using two silica nanotips whose relative positions (i.e., relative phase angle β) and sizes within the evanescent field of the WGMs were controlled by nanopositioners (**Fig. 1**). The size ratio of the scatterers was tuned by enlarging the volume of one of the nanotips within the resonator mode field while keeping the volume of the other nanotip fixed.

The evolution of the eigenmodes of the system was obtained by coupling two waveguides to the system (**Fig. 1& S1**) and monitoring the transmission spectra (**Fig. S3**) as the wavelength of a tunable laser was scanned. The two eigenmodes coalesced clearly as the

phase difference angle β between the 1st and the 2nd nanoscatterer was varied to the vicinity of the EP but bifurcated again as β was further increased. We also checked the evolution of the eigenfrequencies when the effective size of the 2nd scatterer was varied at different phase difference angles β.

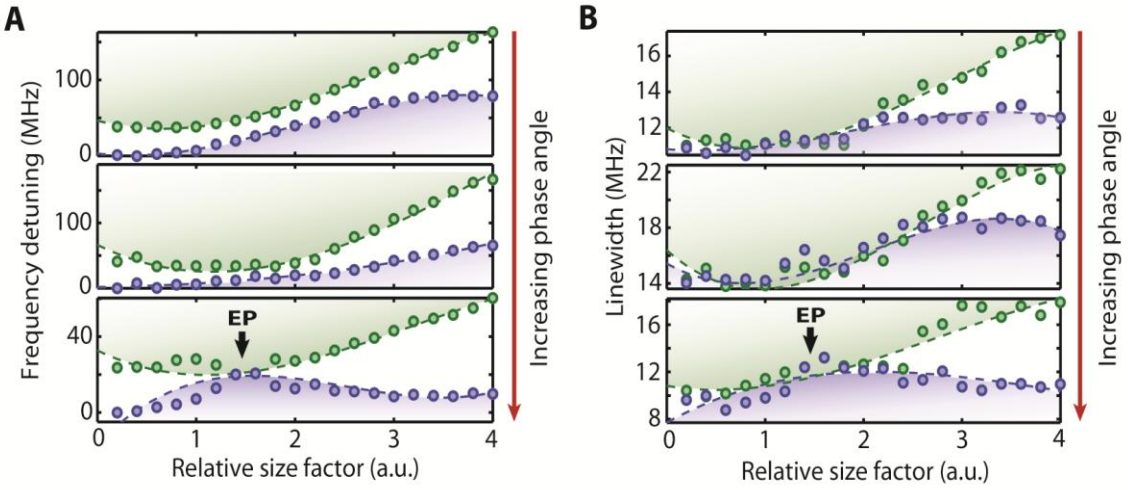

Fig. S4. *Experimentally obtained evolution of eigenfrequencies as the relative size of the scatterers was varied at different relative phase angles β. (A) Difference of the real parts of the eigenfrequencies (frequency splitting or frequency detuning). (B) Imaginary parts (linewidths) of the eigenfrequencies.*

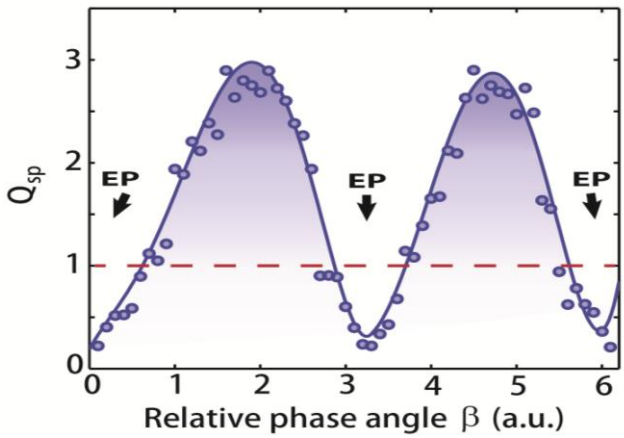

Fig. S5. *Experimentally obtained evolution of the splitting quality factor as a function of β for fixed relative size factor.*

In **Fig.1C** of the main text, we presented the evolution of the frequency splitting *2g*, linewidth difference γ_{diff} and the sum γ_{sum} of the linewidths of split modes as a function of the relative phase angle β. In **Figs. S4 & S5** we provide more experimental results to further clarify how the relative phase angle β and the relative size factor of the scatterers affect the spectra of the split resonance modes and help to drive the system to the vicinity of an EP. **Figure S4** depicts the evolution of the amount of frequency splitting and the linewidths of the split resonances as a function of the size factor at different values β implying that when the relative size factor is varied, the system can or cannot reach an EP depending on the relative phase angle β between the scatterers: For some values of β, the system experiences avoided crossing. The resolvability of the frequency splitting in a transmission spectrum was previously quantified by the splitting quality factor, which is defined as the ratio of the frequency splitting *2g* to the sum γ_{sum} of the linewidths of the split resonances[15]. Experimental results shown in **Fig. S5** clearly show that when the resonances coalesce at an EP, the splitting quality factor reaches its minimum.

S3. Emission and chirality analysis for the lasing cavity

As a consequence of the non-Hermitian character of the Hamiltonian the eigenvectors (S.4) are in general not orthogonal. This happens whenever the backscattering is asymmetric, $|A| \neq |B|$, as $\Psi_+^* \cdot \Psi_- = |A| - |B|$. The asymmetric backscattering $|A| \neq |B|$ also implies that both modes have a dominant component that increases the closer the system is steered to the EP (**Fig. S6**). This corresponds to a dominant propagation direction in real space. We quantify this imbalance by the chirality[6,7]

$$\alpha_{\text{TMA}} = \frac{|A| - |B|}{|A| + |B|} \ . \tag{S.8}$$

In contrast to the original definition of the chirality[1,4,5,8], this chirality parameter also provides information on the sense of rotation not just on its absolute magnitude. For a balanced contribution, $|A| \approx |B|$, the chirality is close to 0. In the case where the CCW (CW) component dominates, $|A| > |B|$ ($|A| < |B|$), the chirality approaches 1 (-1) and both modes become copropagating. By carefully tuning the position of one of the scatterers, it

is possible to create a situation of full asymmetry in the backscattering, i.e. $\alpha \to \pm 1$. In this case, either A or B vanishes, while the other component is nonzero[1]. Solving the Schrödinger Eq. (S.1), we get the eigenfrequencies of the system Eq. (S.3). The corresponding eigenmodes Eq. (S.4) can be further expressed as

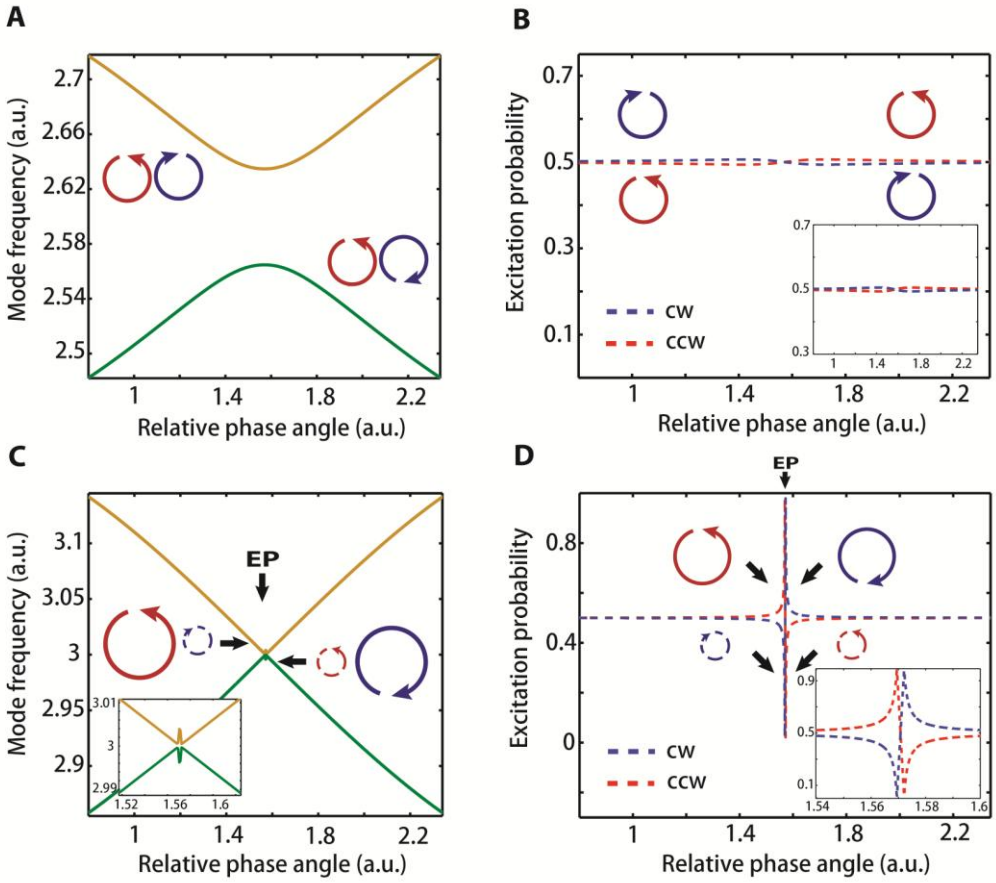

Fig. S6. *Weights of CW and CCW components in the eigenmodes as the relative phase difference β between the two nanoscatterers is varied, away from EP and in the vicinity of EP, with two different size factors of the 2nd nanoscatterer, according to Eq.(S.9). Evolution of the eigenfrequencies and CW (CCW) weights in the eigenmodes as β is varied for (A) and (B) V_1=1.5-0.1i, V_2=1.0997-0.065i, and (C) and (D) V_1=1.5-0.1i, V_2=1.4999-0.104i. Note that for the size factor used in (A) and (B) eigenmodes cannot reach the EP whereas for the size factor used in (C) and (D) the eigenmodes can reach the EP and a strong asymmetric distribution of the CW/CCW weights appears in the vicinity of EP. Insets are the zoom-in plots in the vicinity of EP. In (C) and (D), two EPs are clearly seen.*

$$\Psi_{\pm} = \Psi_{ccw} \pm \sqrt{B/A}\Psi_{cw}. \tag{S.9}$$

In the experiments, the chirality (S.8) of the eigenmodes of the system can be obtained by coupling waveguides to the system (as shown in **Fig. S1**) and by inducing lasing (e.g., Raman lasing in silica resonators or lasing from Erbium ions in Erbium doped silica resonators) within the system. Using coupled mode theory and the assumption that there is no backscattering of light from the waveguide into the cavity one can relate the amplitudes in the waveguide to the coefficients A and B via

$$a_{cw,out} = -\sqrt{\kappa_1}^{*}\Psi_{CW} = -\sqrt{\kappa_1}^{*}\sqrt{B} \tag{S.10}$$

$$a_{ccw,out} = -\sqrt{\kappa_1}^{*}\Psi_{CCW} = -\sqrt{\kappa_1}^{*}\sqrt{A}\ . \tag{S.11}$$

Hence, the chirality of the lasing system can be obtained from the waveguide amplitudes as

$$\alpha_{\text{lasing}} = \frac{\left|a_{ccw,out}\right|^2 - \left|a_{cw,out}\right|^2}{\left|a_{ccw,out}\right|^2 + \left|a_{cw,out}\right|^2}, \tag{S.12}$$

where $a_{ccw,out}$ can be either $a_{1,out}$ or $a_{4,out}$ and $a_{cw,out}$ can be either $a_{2,out}$ or $a_{3,out}$. The same formula can also be used in full numerical calculations to extract the chirality of the quasi-bound states of the system for comparison to the result of the two-mode approximation of Eq. (S.8).

S4. Chirality analysis and comparison between the lasing and the transmission models

In this section we extend the TMA to describe the transmission of light through waveguide-cavity systems as illustrated in **Fig. S1**, which is also the setup for the results and the analysis shown in **Fig. 3** of the main text. We allow for incoming waves from the upper left with amplitude $a_{1,\text{in}}$ and from the upper right with amplitude $a_{2,\text{in}}$, such that it is possible to couple into the WGMs in either the CW or the CCW directions. Based on coupled mode theory we add a coupling term to Eq. (S.1) and arrive at

$$i\frac{d}{dt}\Psi = \mathrm{H}\Psi + i\sqrt{\kappa_1}\begin{pmatrix} a_{2,\mathrm{in}} \\ a_{1,\mathrm{in}} \end{pmatrix} \tag{S.13}$$

with κ_1 denoting the waveguide-resonator coupling coefficient. The losses due to coupling of the cavity to the waveguides are included in the diagonal elements Ω_c of the Hamiltonian (S.2). Assuming that there is no backscattering of light between the microcavity and the waveguides (which is justified when the distance between cavity and waveguides is sufficiently large) we derive the outgoing amplitudes in the lower waveguide as

$$a_{3,\mathrm{out}} = -\sqrt{\kappa_1}^{*}\Psi_{\mathrm{CW}} \tag{S.14}$$

$$a_{4,\mathrm{out}} = -\sqrt{\kappa_1}^{*}\Psi_{\mathrm{CCW}}. \tag{S.15}$$

We can choose κ_1 to be real as we are only interested in the absolute values of $a_{3,\mathrm{out}}$ and $a_{4,\mathrm{out}}$. For a CW excitation with $a_{1,\mathrm{in}}$ at a fixed frequency ω_e we find from Eqs. (S.14)-(S.15)

$$a_{3,\mathrm{out}} = \frac{i\kappa_1(\Omega_c - \omega_e)}{(\Omega_c - \omega_e)^2 - AB}a_{1,\mathrm{in}} \tag{S.16}$$

$$a_{4,\mathrm{out}} = \frac{-i\kappa_1 A}{(\Omega_c - \omega_e)^2 - AB}a_{1,\mathrm{in}} \tag{S.17}$$

Analogously, for a CCW excitation via $a_{2,\mathrm{in}}$ we find

$$a_{3,\mathrm{out}} = \frac{-i\kappa_1 B}{(\Omega_c - \omega_e)^2 - AB}a_{2,\mathrm{in}} \tag{S.18}$$

$$a_{4,\mathrm{out}} = \frac{i\kappa_1(\Omega_c - \omega_e)}{(\Omega_c - \omega_e)^2 - AB}a_{2,\mathrm{in}} \tag{S.19}$$

The asymmetric backscattering expresses itself here by the fact that the numerator of $a_{4,\mathrm{out}}$ in Eq. (S.17) is proportional to A, whereas the numerator of $a_{3,\mathrm{out}}$ in Eq.(S.18) is

proportional to B. Assuming that the input amplitudes $a_{1,\mathrm{in}}$ and $a_{2,\mathrm{in}}$ are the same, we find the chirality as defined by Eq. (S.8) in terms of the transmission amplitudes to be

$$\alpha_{\mathrm{transmission}} = \frac{|a_{4,\mathrm{out}}| - |a_{3,\mathrm{out}}|}{|a_{4,\mathrm{out}}| + |a_{3,\mathrm{out}}|} \tag{S.20}$$

where $a_{4,\mathrm{out}}$ ($a_{3,\mathrm{out}}$) has been obtained by injecting light at port 1 (2). The crucial difference between the formulas for the chirality as measured in the lasing system [Eq. (S.12)] and the formula for the chirality as measured in a transmission experiment [Eq. (S.20)] is that in the former the intensities, $|a|^2$, of the outgoing waveguide modes are used, whereas in the latter only the modulus of the amplitudes, $|a|$, appear.

In order to compare the two different chirality formulas, Eqs. (S.12) and (S.20), we have performed numerical calculations using a finite element method where we have solved the inhomogeneous Helmholtz equation. The calculations were restricted to the transverse magnetic (TM) polarization in two dimensions. The geometry of the system is shown in **Fig.S1**. The parameters for the waveguides and scatterers have been chosen such that the scatterers perturb the eigenvalues of the system much stronger than the waveguides coupled to the resonator. Therefore, the chirality is determined primarily through the scatterers, similar to the experiment. One of the scatterers had a fixed position, situated at an angle of $\pi/2$ with respect to the waveguides. The second scatterer was situated on the opposite side of the disk and its position was given by the angle β between the scatterers. The effective size factor, d_2, of the second scatterer (which is the spatial overlap between the scatterer and the optical mode) was varied by changing the distance between the scatterer and the resonator. In the calculations the angle β was varied between 2.91 and 3.06, and the size factor d_2 was varied between 0.01 and 0.04. The waveguides, as well as the microresonator had an effective refractive index of $n = 1.444$. The system was excited by injecting light into the waveguides at any of the ports 1-4 with frequency ω_e, achieved by placing a line source $f(y)$ at the corresponding side of the system (marked by a black dashed line in **Fig. S1**), which

excites only the fundamental mode $f(y,\omega_e)e^{\pm i\beta_x x}$ of the waveguide. Both, the spatial profile $f(y,\omega_e)$ of the fundamental mode, as well as the propagation coefficient β_x were found through matching conditions at the dielectric waveguide interface[16]. The computational domain was truncated by a reflectionless perfectly matched layer, which absorbs all scattered outgoing waves. The incoming and outgoing amplitudes $a_{1-4,\{\text{in,out}\}}$ of the waveguide modes were extracted by projecting the solution of the inhomogeneous Helmholtz equation onto the individual (fundamental) waveguide modes.

In **Fig. S7** we compare the chirality as determined from the eigenvalue calculations for the lasing cavity with the chirality as determined from the transmission calculations. The chirality is obtained under variation of the two positional parameters (d_2, β) of the second scatterer. We chose to vary two parameters in order to be able to exactly reach the exceptional points where the chirality features an absolute maximum, i.e. $\alpha = \pm 1$. In the

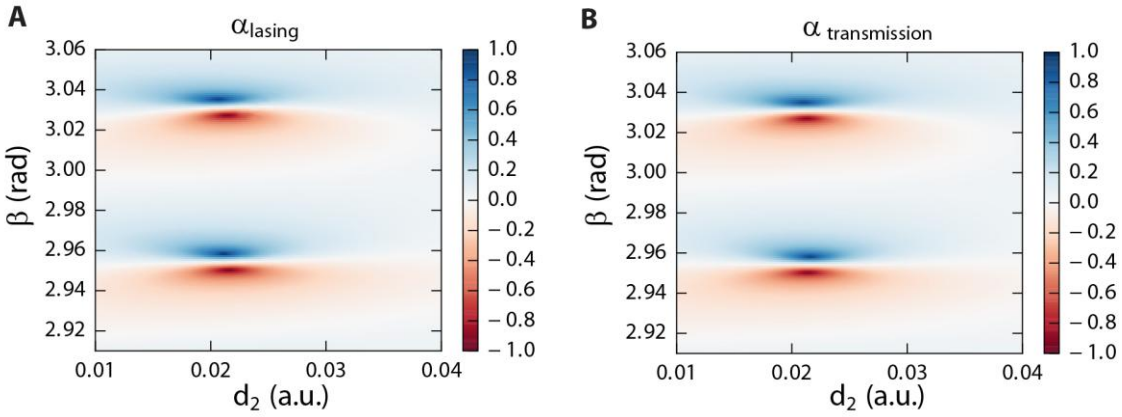

Fig. S7. *Comparison of the chirality obtained (A) through a full numerical eigenvalue calculation by Eq. (S.12) and (B) through a full numerical transmission calculation by Eq. (S.20). The dependence of the chirality is plotted with respect to the position of the second scatterer given by both the angle between the scatterers, β, as well as by the effective size factor, d_2. Both formulas yield very similar values for the chirality validating Eqs. (S.12) and (S.20).*

parameter range shown in **Fig. S7** two pairs of EPs are depicted where each pair features two EPs of opposite chirality. The pattern of EP pairs is roughly repetitive when extending the scanned interval of angle β as long as the scatterer does not come close to one of the attached waveguides. In the calculations we observe an excellent agreement between the two chirality definitions such that we can indeed assume that both methods yield a good estimate for the internal chirality of the whispering gallery modes induced by the presence of the two scatterers.

In a next step we explicitly compared the full numerical results to the results from the TMA model. For this, we calculated the parameters A, B, and ω_c through separate eigenvalue calculations for each of the scatterers, where no waveguides were attached to the system. The value for the coupling coefficient κ_1 has been determined from transmission calculations from port 1 to port 3 with no scatterers present. In **Fig. S8** the chirality definitions of Eqs. (S.8), (S.12) and (S.20) are compared to each other for the case that the distance of the 2nd nanotip is fixed at the same distance as the 1st nanotip, i.e. $d_2 = 0.02$. Similar to **Fig. S7** we again observe an excellent agreement between the

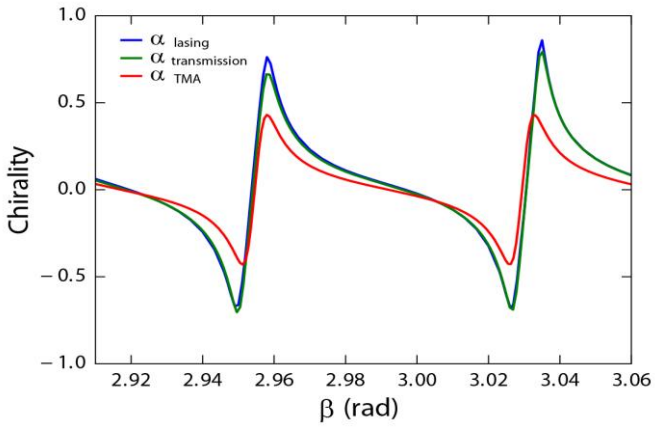

Fig. S8. *Comparison of the chirality definitions for* α_{TMA}, α_{lasing} *and* $\alpha_{transmission}$. *In the calculations the second scatterer has an effective size factor* $d_2 = 0.02$ *and the angle* β *is varied.*

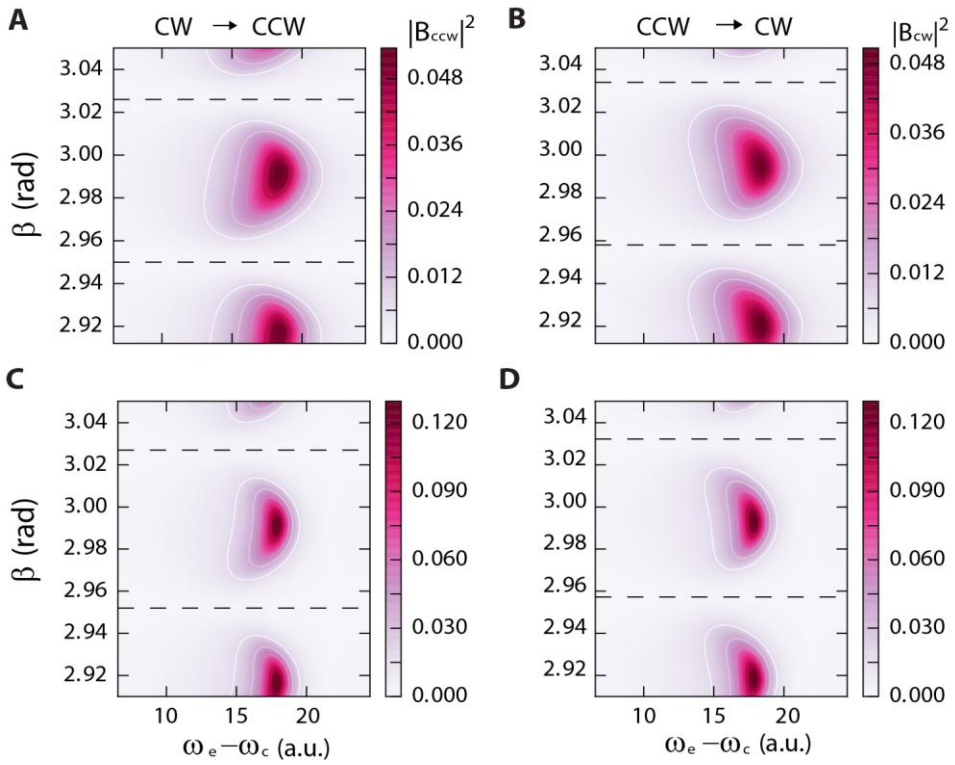

Fig. S9. *Asymmetric backscattering intensities* $\left|B_{CW/CCW}\right|^2$ *from a CW to a CCW wave [left panel: (A) and (C)] and from a CCW to a CW mode [right panel: (B) and (D)]. The results are obtained from a full numerical transmission calculation using a finite element method [upper panel: (A) and (B)], as well as from the TMA model [lower panel: (C) and (D)]. Both models yield the same frequencies at which the backscattering intensities peak, but the overall intensities differ from each other since additional scattering processes as from the waveguide to the resonator are not included in the TMA. In each panel the backscattering intensity is shown as functions of the injected frequency detuning* $\omega_e - \omega_c$ *and the angular position* β *of the second nanotip. Dashed lines mark the local minima of backscattering intensities, corresponding to the chirality maxima and minima. The asymmetric backscattering is shown by the shifted intensity patterns with respect to the angle* β *.*

numerical calculations. For the TMA model we find that it correctly predicts the angles at which the chirality becomes minimal/maximal, but the exact values differ. The reason for

this is that the TMA model does not include other scattering processes as, for example, from the resonator to the waveguide.

The asymmetric backscattering which results in the intriguing chirality behavior in **Fig. S8** can also be observed by looking at the normalized backscattering intensity $|B_{CCW}|^2 = |a_{\mathrm{ccw,out}}|^2 / |a_{\mathrm{cw,in}}|^2$ from the CW to CCW traveling mode and the similarly defined $|B_{CW}|^2$. From Eq. (S.12) it follows that an exceptional point (with an absolute chirality maximum) is reached when either of the backscattering intensities $|B_{CW/CCW}|^2$ is zero. Hence, a chirality maximum (minimum) can be found by minimizing the backscattering intensity $|B_{CCW}|^2$ ($|B_{CW}|^2$). This strategy has also been used in the experiment and the corresponding data is shown in **Fig. 2** of the main text. The EPs corresponding to opposite chiralities occur at slightly different angles β, which manifests itself by shifting the two backscattering intensity pattern $|B_{CW/CCW}|^2$ with respect to the angle β as shown in **Fig. S9**. Here, the angles β at which the backscattering $|B_{CW/CCW}|^2$ becomes minimal are indicated by dashed lines. In addition, both the results for the TMA model and the numerical transmission calculations are plotted. The frequencies at which the backscattering intensities $|B_{CW/CCW}|^2$ peak match very well between the two models; however, the predicted overall intensities differ due to the differences in the models.

S5. Directionality analysis for the biased input case in the transmission model

As discussed in the main text, the intrinsic chirality is different from the directionality when light is injected into the resonator in a preferred direction such as in the CW or the CCW direction (i.e., we referred to this as the biased input). Our experiments described in the main text revealed that varying the relative distance (relative spatial phase) between the scatterers affects the amount of light coupled out of the resonator into the forward direction (i.e., in the direction of the input) and into the backward direction (i.e., in the

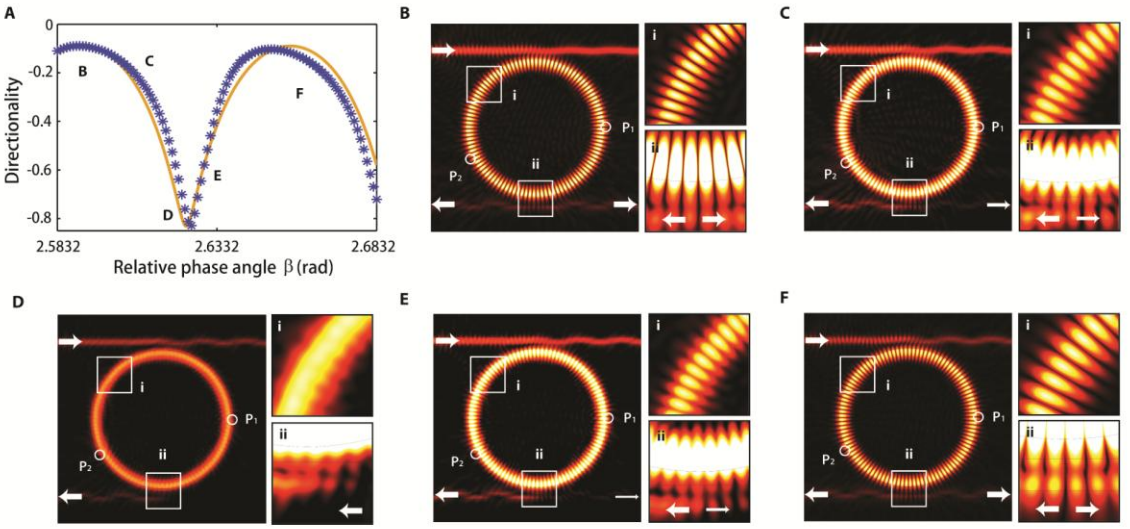

Fig. S10*. Directionality with a biased input (CW) as a function of the relative phase difference between two scatterers (A). Summary of the results obtained in the numerical simulation and the fitting curve using the theoretical model. (B-F), Results of finite element simulations at different relative phase angles β but fixed size factor revealing the intracavity field patterns and output direction in the waveguides. β values are: (B) 2.590 rad; (C) 2.617 rad; (D) 2.625 rad; (E) 2.631 rad; and (F) 2.653 rad. P_1 and P_2 denote the locations of the scatterers.*

opposite direction of the input); however, the amount of light coupled out of the resonator into the forward direction always remains higher than that in the backward direction.

Figure S10 depicts the results of finite element simulations with COMSOL validating our experimental observations presented in **Figs. 2**&**3** in the main text. It is seen that directionality is always negative taking values between its minimum and maximum values by changing the relative phase angle. Decreasing directionality implies the presence of scattering into the direction opposite to the direction of the injected light. Backward scattering, however, remains always weaker than forward scattering. Simulations reveal that when the intracavity field forms a standing-wave pattern with well defined nodal lines, light couples out from the resonator in both the cw and ccw directions (**Fig. S10B**); however, when nodal lines are washed out and the field profile

deviates from the standing-wave pattern light couples out from the resonator in the direction of the input (**Fig. S10D**). A relation between the visibility of the nodal lines (and the standing-wave pattern) and the ratio of the light coupled into cw and ccw directions is clearly seen (**Fig. S10**).

References:

1. J. Wiersig, Structure of whispering-gallery modes in optical microdisks perturbed by nanoparticles. *Phys. Rev. A*. **84**, 063828 (2011).
2. M. V. Berry, Physics of Nonhermitian Degeneracies. *Czechoslov. J. Phys.* **54**, 1039–1047 (2004).
3. T. Kato, Perturbation Theory for Linear Operators (Springer, 2008), *Springer Classics in Mathematics*.
4. J. Wiersig, Chiral and nonorthogonal eigenstate pairs in open quantum systems with weak backscattering between counterpropagating traveling waves. *Phys. Rev. A*. **89**, 012119 (2014).
5. J. Wiersig et al., Nonorthogonal pairs of copropagating optical modes in deformed microdisk cavities. *Phys. Rev. A*. **84**, 023845 (2011).
6. M. Kim, K. Kwon, J. Shim, Y. Jung, K. Yu, Partially directional microdisk laser with two Rayleigh scatterers. *Opt. Lett.* **39**, 2423–2426 (2014).
7. H. Schomerus, J. Wiersig, Nonhermitian transport effects in coupled-resonator optical waveguides. *Phys. Rev. A*. **90**, 053819 (2014).
8. J. Wiersig, S. W. Kim, M. Hentschel, Asymmetric scattering and nonorthogonal mode patterns in optical microspirals. *Phys. Rev. A*. **78,** 053809 (2008).
9. W. D. Heiss, Repulsion of resonance states and exceptional points. *Phys. Rev. E*. **61**, 929-932 (2000).
10. W. D. Heiss, Exceptional points of non-Hermitian operators. *J. of Phys. A:Math. and Gen.*, **37**, 2455 (2004).
11. A. Taove, and S. C. Hagness, Computational Electrodynamics: The Finite difference Time-domain Method. Artech House (2005).

12. J. Wiersig, Boundary element method for resonances in dielectric microcavities. *J. of Opt. A: Pure and Appl. Opt.* **5**, 53-60 (2003).
13. C. P. Dettmann, G. V. Morozov, Sieber, M., and Waalkens, H. Unidirectional emission from circular dielectric microresonators with a point scatterer. *Phys. Rev. A.* **80**, 063813 (2009).
14. D. Braess, Finite Elemente: Theorie, schnelle Loser und Anwendungen in der Elastizitatstheorie. Springer-Verlag (2013).
15. S. K. Ozdemir, J. Zhu, L. He, and L. Yang, Estimation of Purcell factor from mode-splitting spectra in an optical microcavity. *Phys. Rev. A* **83**, 033817 (2011).
16. J. D. Jackson, Classical Electrodynamics. Wiley (2007).